Classical and Quantum Gravity

Crystallite growth limits in amorphous oxides

OPEN ACCESS
IOP Publishing
Classical and Quantum Gravity
Class. Quantum Grav. **41** (2024) 025003 (16pp)
https://doi.org/10.1088/1361-6382/ad14b7

Crystallite growth limits in amorphous oxides

Seth Linker[1,2,3,*], Christopher Ausbeck[4], Riccardo DeSalvo[1,5], Veronica Granata[1,2,6], Brecken Larsen[7], Tugdual LeBohec[4], Yangyang Liu[3], Akilah Miller[8], Marina Mondin[3], Joshua Neilson[1] and Harry Themann[3]

[1] University of Sannio at Benevento, C.so Garibaldi 107, Pal. dell'Aquila Bosco-Lucarelli, I-82100 Benevento, Italy
[2] INFN, Sezione di Napoli Gruppo Collegato di Salerno, Salerno, Italy
[3] California State University Los Angeles, 5151 State University Drive, Los Angeles, CA 90032, United States of America
[4] University of Utah, 115 South 1400 East, Salt Lake City, UT 84112, United States of America
[5] RicLab, 1650 Casa Grande Street, Pasadena, CA 91104, United States of America
[6] University of Salerno, Via Giovanni Paolo II, 132, 84084 Fisciano, SA, Italy
[7] University of Arizona, 1200 E University Blvd, Tucson, AZ 85721, United States of America
[8] University of Illinois Urbana-Champaign, 506 S. Wright St, Urbana, IL 61801, United States of America

E-mail: slinker2@calstatela.edu

Received 21 August 2023; revised 5 December 2023
Accepted for publication 12 December 2023
Published 22 December 2023

Abstract

Post deposition thermal annealing of amorphous coatings improves optical properties of dielectric mirrors. However, excessive temperatures cause crystallization, resulting in a degradation of mechanical and optical properties. Therefore, annealing is limited to temperatures 'below' the crystallization threshold. The threshold is determined by x-ray diffraction (XRD) measurement which requires a significant amount of crystallized material for detection, yet it has been shown that a population of crystallites may exist in otherwise amorphous coatings below the threshold temperature. In this study XRD measurements show crystallites that grow during annealing within amorphous

* Author to whom any correspondence should be addressed.

oxide coatings to a limited and predictable size predicated on the difference in density between the crystal and the surrounding amorphous phase and the average material's Young's modulus. These crystallites may be the point-like, extremely weak scatterers revealed in the LIGO test masses when imaged off-axis.

Supplementary material for this article is available online

Keywords: crystallites, gravitational waves, optical coatings, scatter, zirconia, titania, XRD

1. Introduction

Interferometric gravitational wave detectors TAMA (Ando 2005), GEO (Grote 2010), Virgo (Acernese *et al* 2014), LIGO (Harry 2010) and KAGRA (Aso *et al* 2013) require test masses (mirrors) with highly reflective dielectric coatings with alternating layers of high and low index of refraction. Amorphous dielectric films must be annealed after deposition to optimize their optical and mechanical loss properties, which improve with increased temperature up to a point (Harry 2012). If annealed at too high of a temperature, the amorphous material crystallizes, which leads to a degradation of these properties (Lv 2018). Therefore, the optimal annealing temperature is set by the 'crystallization threshold temperature' (Martin *et al* 2010), which is usually determined by x-ray diffraction (XRD) measurements. The issue in XRD determination of the crystallization threshold is that the method requires a sufficient volume of crystalline material for detection. There are examples of transmission electron microscope (TEM) images which show crystallites in otherwise amorphous films below the crystallization threshold determined in the same study by XRD (Sengottaiyan *et al* 2019). A small population of crystallites may therefore be present in all mirrors (Glover *et al* 2018).

We performed a study of the two high-index amorphous oxides titania (TiO_2) and zirconia (ZrO_2), focusing on the effect that annealing has on crystallization. XRD analysis of the samples shows that crystallites form during annealing (zirconia showed crystallization immediately following deposition), with a material-specific maximum size. The crystallites always appear as grown to their maximal size at the crystallization threshold temperature, while higher temperature annealing appears to increase only their number. In some cases, annealing at much higher temperatures eventually results in an increase of the crystallite size. A fraction of the material in the amorphous phase does not crystallize at the temperatures and annealing times we tested. The measured values for the fraction of remaining material for titania and zirconia are presented in the results section.

The sub-wavelength scale of these crystallites with relative refractive index typically <1 makes them very weak light scatterers (Hulst 1957). They appear as good candidates for the millions of scatterers observed by Glover off-axis images of the LIGO test masses illuminated by the stored light beam.

We first detail the method used to deposit the coating samples, the annealing procedure and the XRD analysis used to measure crystallite size and the fraction of crystallized material. Then the results are presented for the threshold temperatures and the crystallite sizes. We next propose a mechanism which may be responsible for restraining the crystallite growth. This would result from the shrinkage-induced stress at the periphery of forming crystallites. With respect to crystallite size, it takes the form of a 4th order term added to the standard Gibbs free

energy expression for otherwise unrestricted crystallite growth. The maximum crystallite sizes predicted by this expression are found to be in quantitative agreement with the observed results for the two materials studied. Similar, but less accurate measurement on tantala coatings were found to be not incompatible with the results presented here. Following the conclusion, we discuss the scattering power of a population of crystallites with the observed size and compare it with the power scattered from a detector test mass.

2 Procedures and methodology

For all the samples presented in this paper, metal oxide targets (at least 99.99% nominal purity) were electron beam evaporated from crucibles in a chamber with a base pressure of 10^{-4} mbar, and gas flow rates for oxygen and argon of 20 sccm and 5 sccm respectively. During the evaporation process, the adatoms were continuously bombarded by an argon ion beam directed onto the surface of the substrates. The evaporated atoms and molecules feature kinetic energies much less than 1 eV which is not enough to form dense layers. The bombardment with ions from an argon source deposits enough energy into the sample surface to allow for diffusion of the adatoms into a denser arrangement (Nastasi 1996). The deposition rate was monitored by a quartz crystal monitor. Following deposition, the total thicknesses were verified at the edges of masked patterns with a Dektak stylus profilometer. The set of samples manufactured and studied are presented in table 1. More technical details for the coating procedure can be found in a PhD thesis, (Neilson 2022).

The coating samples were deposited at room temperature onto 1 mm thick, 25 mm diameter, (100) c-Si (Siltronix n.d.) substrates which fit into a Bruker D-2 benchtop diffractometer for Bragg–Brentano θ–2θ XRD measurement. Some polished fused silica substrates of the same dimensions were used for optical measurements of the coatings. The crystalline silicon wafer substrates were chosen to depress the large continuum background in the XRD measurements present with amorphous substrates and thus improve sensitivity to the amorphous fraction of the coating material. Results from both the glass and c-Si substrates are presented.

The effects of detector noise in the XRD data on the determination of the onset of crystallization were quantified by adding an artificial Gaussian signal of width matched to that of the diffraction peaks in crystallized samples to a region containing only baseline signal. It was found that a fit with a significance of 3 sigma can be made only if this added signal is at least 3%–5% the height of the largest experimentally observed peaks. Diffraction peaks from crystallized material, which are less than 3%–5% of the fully crystallized signal, remain indistinguishable from the background noise.

Samples were measured with XRD in their ‘as deposited’ state and then after each annealing step, at progressively higher temperatures, to monitor the evolution of crystallization. Annealing was carried out in air. The soak temperature was reached with a ramp of 3° min^{-1} and then held for 24 h. The samples were then allowed to cool down to room temperature in the oven. The temperature steps between annealing cycles were changed to reduce the time of the experiment or to optimize the sensitivity to the crystallization transition.

The size of the crystallites in the direction perpendicular to the coating layers was calculated from the width of the scattering peaks using the Scherrer equation,

$$\tau = \frac{K\lambda}{B\cos(\theta)}, \tag{1}$$

where λ, K, B, and θ represent the wavelength of the x-ray source, the shape factor, the full width at half maximum (FWHM) of the peak, and the diffraction angle location of the peak

Table 1. Gives the thicknesses and materials of the samples deposited for this study along with their respective substrates. Sample A and B are nominally identical titania films.

Total thickness (nm)	ZrO_2		TiO_2		Substrate
	Number of layers	Layer thickness (nm)	Number of layers	Layer thickness (nm)	
104 ± 5.2	0	0	1	100 ± 5.0	Fused silica
204 ± 3.2	0	0	1	200 ± 3.0	Fused silica
300 ± 5.0	0	0	1	300 ± 5.0	Silicon (Sample A)
300 ± 5.0	0	0	1	300 ± 5.0	Silicon (Sample B)
204 ± 5.2	1	200 ± 5.0	0	0	Fused silica
300 ± 5.0	1	300 ± 3.0	0	0	Silicon
300 ± 6.0	2	100 ± 2.0	1	100 ± 2.0	Silicon
300 ± 6.0	1	100 ± 2.0	2	100 ± 2.0	Silicon

respectively. The FWHM will be affected by instrumental line broadening and these effects were quantified by measuring the width of the silicon mono-crystal diffraction peaks. The c-Si FWHM was subtracted from the FWHM of the diffraction peaks of the coating material prior to calculating the crystallite sizes reported here.

The Bruker diffractometer generates x-rays with a wavelength $\lambda = 0.154$ nm using a Cu target. The shape factor, K depends on the morphology of the crystallite can range from ~1.0 to 1.4 depending on the orientation and shape of the crystal. Since it was not known precisely how the crystals would grow in the films, we used the shape factor provided in literature (Langford *et al* 1978) for a spherical crystallite, $K = 1.07$. This value is consistent with the explanation we propose for the limitation in crystal growth. The range of possible shape factors is incorporated into the error of the data. Furthermore, the crystallite can grow with random orientation if the crystal size remains much smaller than the film thickness, and if nucleation sites are randomly distributed throughout the coating. Therefore, measurements made in a direction can be considered representative of all directions.

The magnitude of the error bars presented in the graphs for the crystallite sizes were calculated from the error in the fit parameters, and (as mentioned in the previous paragraph) from the range of possible shape factors.

For the samples deposited on c-Si, the flat XRD profile measured on the uncoated side was subtracted from the measurement of the coated side. The widths of the diffraction peaks were determined by fitting the data to the product of a Gaussian and Lorentzian function (David 1986). The deposited films were much thinner than the penetration depth of the x-ray beam. In the case of the fused silica substrates, proper subtraction could not be performed due to the large background from the amorphous substrate and deposited silica layers. In this case a simple polynomial term was used in the fit to account for the background signal. The 300 nm thick single titania samples, named ‘A’ and ‘B’ in table 1, are nominally identical. Sample B was annealed with smaller progressive steps in temperature to place a narrower bound on the crystallization threshold temperature.

For each measurement on silicon wafers, both the coated and uncoated sides of the sample are scanned with the XRD. All fits were performed after subtracting the profile acquired on the back side. The fraction of amorphous material remaining at progressive annealing temperatures was determined by measuring a constant 2θ range of acquisition ($15^\circ \rightarrow 60^\circ$ in 2θ) and fitting a Gaussian to the XRD data. The integral of the Gaussian over that range was then taken as a measure of the amorphous material and compared with the ‘as deposited’ value

(measured in the same way) to calculate the remaining fraction at a given annealing temperature. When present, the crystalline peaks were accounted for in the fit with the additional functions mentioned in the previous paragraph. We observed unexpected day-to-day fluctuations in the integrated diffraction count (referred to from now on as the *area*) of the backside scans, which we attributed mostly to changes in the energy threshold of the x-ray detector. Similar fluctuations were observed in some of the amorphous component measurements on the coated sides, that caused large error bars in the amorphous phase. It should be noted that changes in energy threshold in the x-ray detector do not significantly affect the crystalline peaks because the x-rays scattered at those specific angles are monochromatic. Instead, the shape of the continuum below is affected by the threshold in the detector of x-rays because of the fraction of the continuum x-rays that has suffered Compton emission. Peak area measurements may vary with drifts in the power of the source of the diffractometer. This problem is mitigated by performing measurements on a reference sample after each sample measurement.

The sum of the areas of the narrow diffraction peaks can be used as a measurement of the fraction of the coatings that crystallized (Jian and Hejing 2003). Yet, since crystallized matter is formed at the expense of the amorphous material, the amplitude and total area of the Gaussians describing the amorphous material should diminish when the portion of crystallized material increases. The results we present for fractional amount of amorphous material are calculated from the direct observations of the fit to the data for the amorphous signal at progressive annealing steps, not by comparison between the integrated areas of the amorphous and crystalline peaks.

3. Experimental results

The samples listed in table 1 were studied, focusing on crystallite sizes, and crystallized or amorphous fraction as a function of annealing temperature. The key point of the results is that limited crystal sizes are observed while a fraction of the amorphous phase always survives crystallization.

3.1. Zirconia and zirconia-titania coatings

The peak widths and areas were measured for the two peaks of zirconia at $2\theta = 30^{\circ}$ and $2\theta = 35^{\circ}$. These peaks correspond to the crystal planes (111) and (200) respectively. Comparison of the diffractograms with independent published XRD measurements of deposited thin ZrO_2 films suggests that the material crystallized into the Cubic (Fm3m) or Tetragonal ($P4_2/mnm$) phase (Ramirez *et al* 2008). Figure 1 illustrates the fitting procedure and results are displayed from figures 2–5.

The contribution from the amorphous phase for the 300 nm thick samples was evaluated by fitting a Gaussian function after subtracting of the un-coated silicon crystal backside. Figure 1 and the leftmost data points in figure 2 show that the sample was already partially crystallized at deposition while maintaining a significant amorphous component. As annealing progresses up to ∼700 °C the crystalline fraction grows while the amorphous component decreases but never completely disappear. Comparing the amorphous peak's area at deposition and after annealing (figure 2), 41 ± 8% of the amorphous material that had not already crystallized at deposition remained amorphous throughout the annealing procedure.

All the zirconia layer samples showed crystallization immediately at deposition. The maximum zirconia crystallite size evaluated with the Scherrer equation is ∼15 nm.

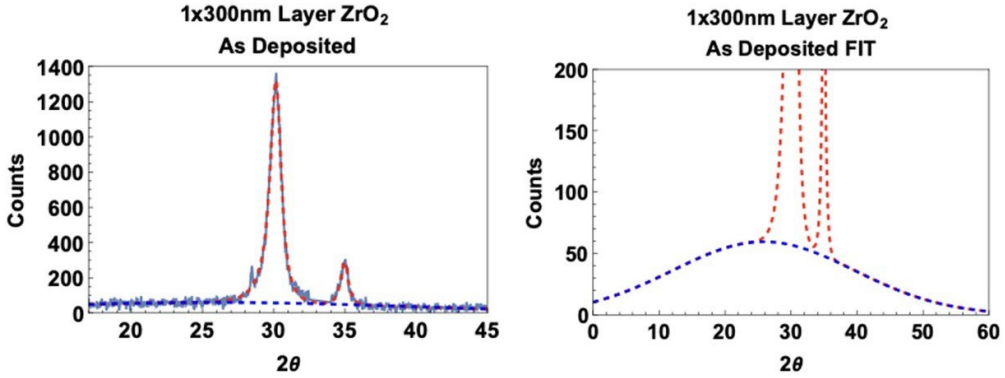

Figure 1. Left image is an example fit to both the crystalline and amorphous components of the unannealed, 300 nm single layer ZrO_2 sample deposited onto silicon. Background from c-Si substrate has been subtracted. Detailed in the image on the right.

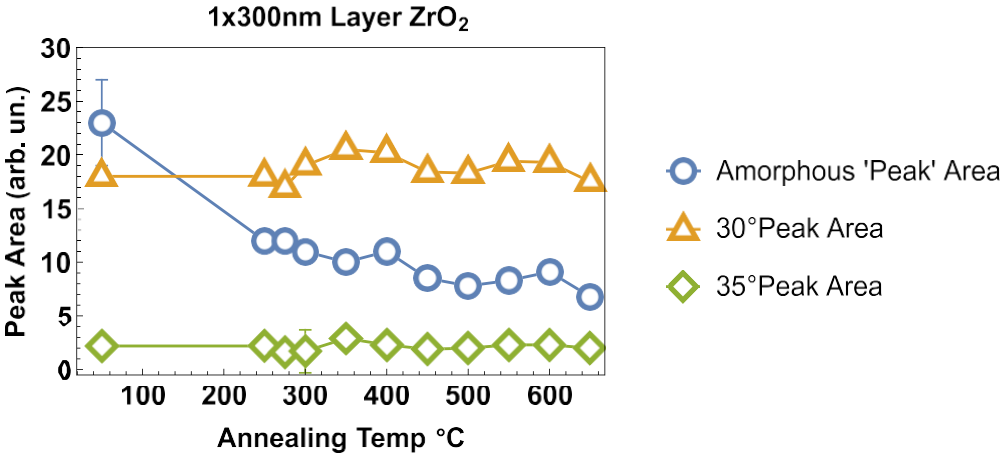

Figure 2. Plot of the progression of the normalized areas of the amorphous and crystalline phase observed for the 300 nm zirconia layer. The error bars were calculated from the fit parameters and are mostly too small to see in the plot.

The titania contribution in the two titania/zirconia samples crystallized at ~250 °C and showed crystallite size of the order of 50 nm, like those observed in the pure titania samples presented in the next section. The slow upward progression of peak area as the annealing temperature increases suggests that amorphous material is still present when the crystallites have attained their maximum individual sizes and number.

Thecrystallite sizes for the 'as deposited' coatings were measured to be around 9 nm (figure 3 left column) for the peak at $2\theta = 30^{\circ}$ and 15 nm (figure 3 right column) for the $2\theta = 35^{\circ}$ peak. The peak at 30° showed a growth in crystallite size by a further 3 nm once the annealing temperature reached ~700 °C. Before that temperature, the samples (which crystallized upon deposition) show fixed crystallite size. The peaks at 35° shows flat crystallite size over the entire annealing range for all the samples. The decreasing trend for the 30° peak area

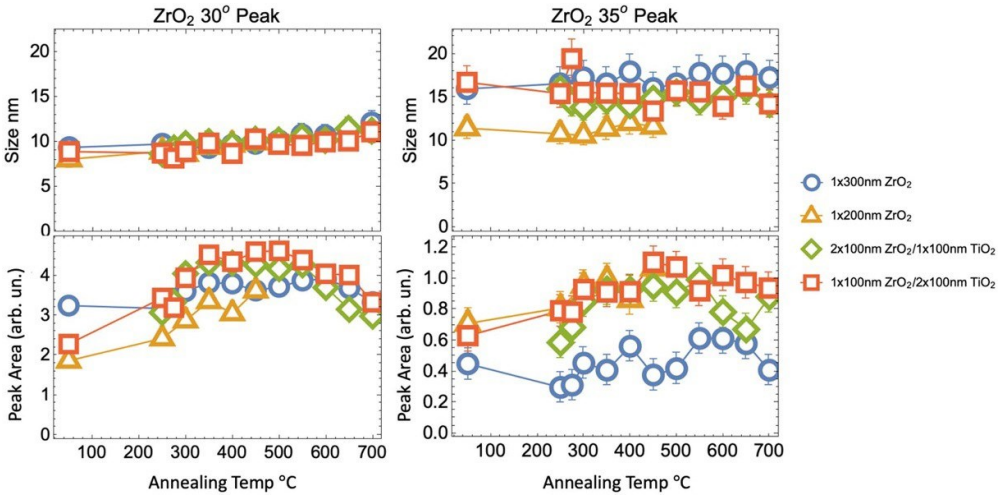

Figure 3. Crystallite sizes (top) and peak areas (bottom) for zirconia (111) (left) and (200) (right). The leftmost data points illustrate pre-annealing crystallization of the thicker samples.

after 550 °C is likely a result of subtraction from the background which showed an increasing trend due to fluctuations in the XRD detector's energy threshold. The trend (although more subtle) is also seen in the peak areas on the right side of figure 3 which were of lower amplitude.

32 *Titania coatings*

The XRD profile for the crystallized samples of deposited TiO_2 corresponds with results in literature for the anatase phase (tetragonal in space group $I4_1/amd$). Measurements of crystal size from both the $2\theta = 25^\circ$ (101) and $2\theta = 38^\circ$ (004) peaks agree within errors. The 38° peak for the 100 nm sample was consistently of low amplitude with respect to the background and resulted in fits for the width with greater error. This is also observed for the lowest temperature 25° and 38° peaks of the 300 nm sample 'B', where the crystallization threshold was observed.

In the range of the annealing temperature threshold for observing crystallization with our XRD setup, all the samples crystallized immediately to their largest measured sizes (within error bars, upper plots) and amounts (peak areas in the lower plots) shown in figure 4.

In three of the four measurements, the crystallization threshold was overshot because the first annealing temperature was too high. For the single 300 nm layer titania sample 'B', measurements were performed with annealing temperature steps of 20 °C to observe the crystal growth rate. Up to 200 °C only the broad diffraction hump from the amorphous phase is visible. A small crystalline peak first appears after the 220 °C annealing emerging from the diffraction signal of the amorphous phase. The size of the crystals and the area of the peaks which appear at that threshold are the lowest temperature data points (triangles) in figure 4. After annealing the coating at 230 °C, the diffraction peak amplitude is dramatically larger after which it does not progress any further. The crystallization process appears to complete within a 10 °C window. The amorphous component has decreased but has not disappeared.

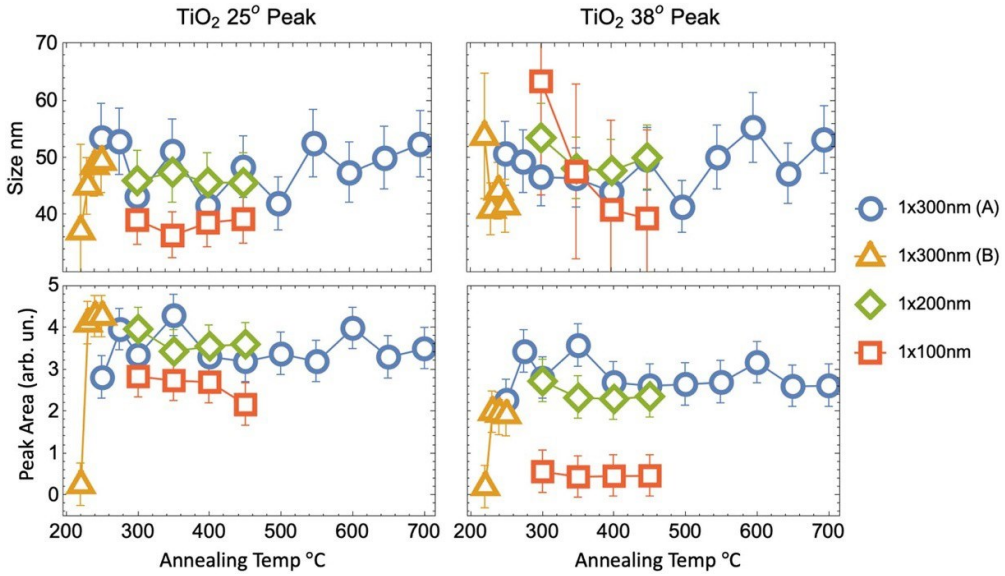

Figure 4. Crystallites sizes (top) compared with diffraction peak area (bottom) as a function of annealing temperature from the dimensions of the (101) (2θ = 25°) and (004) (2θ = 38°) anatase peaks for the samples of table 1.

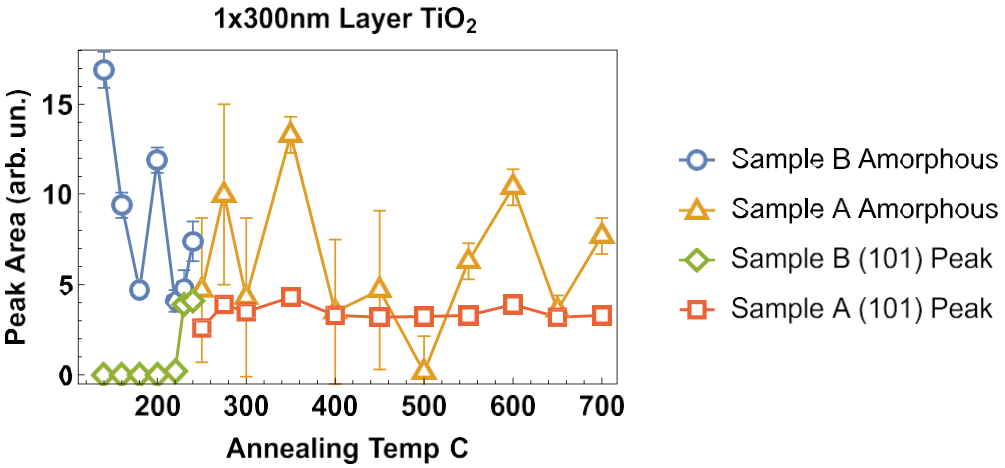

Figure 5. Integrated area of the amorphous contribution compared with the area of the crystallized (101) peaks for the single 300 nm titania layer samples as a function of annealing temperature. The significant fluctuation in the data is discussed in the text.

The fraction of amorphous material which remained after successive annealing treatments was monitored. The values measured for the Gaussian fit to the amorphous area have unexpectedly large fluctuations but in this set of measurements similarly large fluctuations were found in the monocrystalline silicon back side, supposedly for detector instabilities. The results are shown in figure 5. Despite the fluctuations a clear difference is found between the mean peak area prior to crystallization 8.7 ± 1.6, and 6.2 ± 1 at temperatures above the crystallization

threshold at 220 °C. The amorphous fraction drops to 71 ± 18% of initial value but never close to zero. One should not compare the numerical value for area of the crystalline peaks and for the amorphous component in figure 5 because the two scales have different normalizations.

The analysis of the peak widths yields the maximum crystallite size on the order of roughly 50 nm. This value for crystallite size is referenced later when discussing the limiting size model due to the Gibbs free energy.

4. Summary of experimental results

The key points are:

(1) The observation of crystal sizes smaller than that of the thickness of the host layer and which remain constant or almost constant with the annealing temperature.
(2) Measurement of an amorphous component which does not completely vanish upon progressively higher annealing temperatures.

The Scherrer crystal size of crystallites is measured in the direction perpendicular to the coating film. When the layer thickness is much larger than the crystallite size there is no preferred direction for crystal growth and a mechanism limiting growth would apply in all directions. Therefore, we assume that crystallites have the measured size in all directions.

A summary of the averages for the observed maximum crystallite sizes at the crystallization threshold with standard error is presented in table 2.

Some early measurements were also made of e-beam deposited 100 nm and 300 nm layer Ta_2O_5 coatings. More careful analysis needs to be done; however, they appear to show constrained crystallite sizes of ∼70 nm (table 2) at the crystallization threshold with a remaining fractional component of amorphous material, consistent with some recent results from an independent study (Favaro 2023).

5. Gibbs energy model for limited crystallite size

The observation of a limited crystallite size is in contrast with expectations based on the standard expression for the Gibbs free energy. The Gibbs crystallite's size r (equation (2)) has a lower but no upper limits (Nie *et al* 2015),

$$\Delta G = 4\pi\gamma r^2 + \frac{4}{3}\pi\mu r^3. \tag{2}$$

The two constants, γ and μ, represent the surface tension and the volume energy density respectively. The positive γ term is the energetic cost for generating a crystal-amorphous interface, while the negative μ term illustrates the energy gain when the crystal grows volumetrically. The maximum of this function generates the critical size beyond which the crystal will grow indefinitely.

According to the Gibbs formula, once crystallization starts it should progress, and even accelerate due to the increasing volume to area ratio. The fact that crystallite size measurements plateau to the diameters ($2r$) presented in table 2 is therefore surprising.

Normally crystal growth stops when crystals have consumed all available material surrounding them. And then, if there is sufficient mobility, large crystals start cannibalizing the small ones. Since there is evidence of an ample reservoir of amorphous material available surrounding the crystallites even after crystallization has completed, and crystal sizes appear to be

Table 2. Summary of average maximum crystallite sizes measured for coating thickness range of 100–300 nm. Tantala sample results are in italics to denote they are from an earlier, less precise study.

Coating material	Phase	Average maximum size (nm)
TiO_2	Tetragonal	46 ± 5.7
ZrO_2	Cubic/tetragonal	12 ± 3.7
Ta_2O_5	*Hexagonal/orthorhombic*	*71 ± 12*

stalled, an external force must be preventing growth beyond the observed maximum crystallite sizes.

The Gibbs formula was developed to describe crystals growing from a molten environment. We identified a simple mechanism that limits the size of crystallites growing inside an amorphous, but rigid phase when the crystalline phase is denser than the amorphous one. This is the case in all three materials studied. A crystallite growing to unlimited size would eventually generate an empty gap around its boundaries. Before this happens, an energetically expensive strained layer forms around the crystallite, that slows down and then stops its growth.

6. Evaluation of the effect

In the course of crystallization, a volume of uncrystallized (amorphous) material with radial size r_a will shrink to a smaller volume (crystal) with radial size r. Since the amorphous matrix is rigid, if the density of the crystal phase, ρ_c is greater than that of the amorphous, ρ_a, a shell of strain with thickness dr must form around the receding crystallite, as illustrated in figure 6.

The strain can be related to the volume of the crystallite inside the original amorphous phase it grew out of. To evaluate the strain, we take the ratio of the volume of the crystallite and that same volume plus the strained shell,

$$\frac{\rho_c}{\rho_a} = \left(\frac{r_a}{r}\right)^3 \approx \frac{\frac{4}{3}\pi r^3 + 4\pi r^2 dr}{\frac{4}{3}\pi r^3}. \tag{3}$$

The strain, dr is proportional to the crystallite size:

$$dr = \left(\frac{\rho_c}{\rho_a} - 1\right)\frac{r}{3}. \tag{4}$$

An effective spring constant k for the strained bonds between the two volumes is first expressed in terms of the Young's modulus, Y of the coating (bulk) and the dimensions of a mesh element on the surface of the crystallite,

$$k = Y\frac{A}{s} \tag{5}$$

where s is chosen to be on the order of a typical interatomic spacing and A is the area of the surface element. It should be noted at this point that the choice for the value of the Young's modulus to use for the interface (that of the surrounding bulk or for the crystal itself) is not well defined. Fortunately the Young's modulus of the amorphous and crystalline phases of a material are similar, and it is reasonable to use whichever is available in literature. The integration

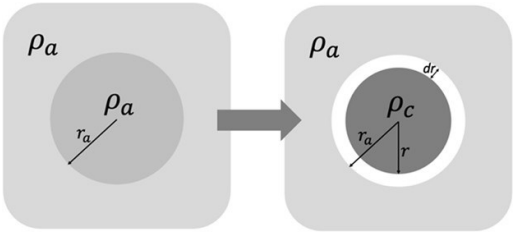

Figure 6. Illustration of the strain layer which forms due to the greater density of the crystal phase forming inside a rigid amorphous phase during crystallite growth.

of the spring potential energy over the surface of the crystallite is then,

$$E_{\text{Shell}} = \frac{1}{2} k dr^2 \left(4\pi r^2\right) \sigma, \tag{6}$$

with σ defined as the density of 'springs' per unit area, which cancels the element area from equation (5), making the choice of element size irrelevant,

$$\sigma \equiv \frac{1}{A}. \tag{7}$$

Substituting (4) and (5) into (6)

$$E_{\text{Shell}} = \frac{1}{2}\frac{Y}{s}\left[\left(\frac{\rho_c}{\rho_a} - 1\right)\frac{r}{3}\right]^2 \left(4\pi r^2\right). \tag{8}$$

And defining the positive coefficient, β

$$\beta \equiv \frac{2Y\pi}{9s}\left(\frac{\rho_c}{\rho_a} - 1\right)^2. \tag{9}$$

Yields a positive 4th order term to be added to the Gibbs free energy (2),

$$E_{\text{Shell}} = \beta r^4. \tag{10}$$

The modified Gibbs energy now accounts for the strain between the crystal the amorphous phase it grew from,

$$\Delta G = 4\pi\gamma r^2 + \frac{4}{3}\pi\mu r^3 + \beta r^4. \tag{11}$$

This new form of the Gibbs free energy expression radically changes the expectations for crystallite sizes. The positive fourth order term requires a stable energy state for the crystal beyond the usual critical size. A comparison of the two formulations calculated using values of physical parameters (γ, μ, ρ_c, ρ_a, Y) found in literature for zirconia is shown below. The maximum of this function occurs at the critical size, the minimum is located at a new predicted 'maximum' size for the crystallite. In the following section we compare the predicted maximum crystallite sizes ($2r_{\max}$ from figure 7) with our observations from XRD.

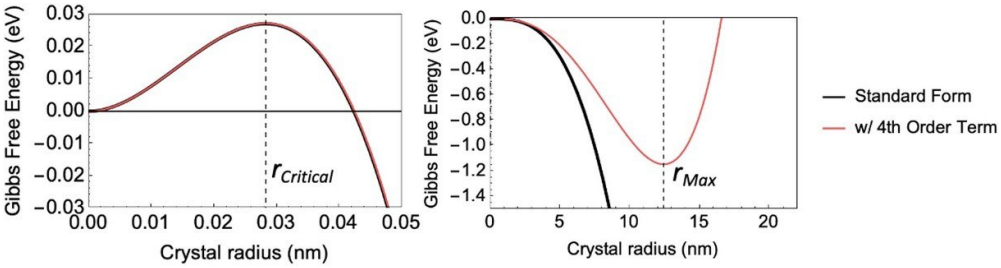

Figure 7. Compares the standard Gibbs free energy expression with the modified one that includes the novel 4th order term. The two curves presented are calculated for zirconia. The prediction of the critical size (vertical dashed line left plot) does not change with the added term, but a new minimum appears requiring a maximum crystallite size (vertical dashed line in right plot).

Table 3. Values used for the coating densities and Young's moduli used to predict the maximum crystallite sizes for zirconia (Koski *et al* 1999), titania (Ottermann *et al* 1996) and (Anderson *et al* 1997), and tantala (Granata *et al* 2020) using the modified Gibbs free energy expression, equation (11).

Material	ρ_c (g cm^{-3})	ρ_a (g cm^{-3})	Y (GPa)	Predicted max size (nm)
ZrO_2	6.1 (tetra.)	5.13 ± 0.5	220 ± 9	16 ± 0.7
ZrO_2	6.1	5.13 ± 0.5	192 ± 9	18 ± 0.9
ZrO_2	6.21 (cubic)	5.13 ± 0.5	220 ± 9	13 ± 0.7
ZrO_2	6.21	5.13 ± 0.5	192 ± 9	15 ± 0.8
TiO_2	3.9 (anatase)	3.0 ± 0.06	66.5 ± 3	22 ± 3.4
TiO_2	3.9	3.0 ± 0.06	65 ± 3	23 ± 3.6
TiO_2	3.9	3.3 ± 0.06	100.5 ± 3	40 ± 4.1
TiO_2	3.9	3.34 ± 0.06	102 ± 3	47 ± 4.7
TiO_2	3.9	3.34 ± 0.06	88 ± 3	54.3 ± 6.3
Ta_2O_5	8.2 (β)	7.04 ± 0.09	117 ± 1	41 ± 0.7
Ta_2O_5	8.37 (α)	7.33 ± 0.06	117 ± 1	55 ±1.0
Ta_2O_5	8.37	7.4 ± 0.03	121 ± 2	62 + 1.2
Ta_2O_5	8.37	7.47 ± 0.09	121 ± 2	74 ± 1.4
Ta_2O_5	8.2	7.33 ± 0.06	117 ± 1	79 ± 1.5

7. Comparison of the model with experimental results

The second order term of equation (11) depends only on the surface energy γ. The value for this parameter was found to be similar for each of the materials (~2 J m^{-2}) (Youhong *et al* 2003, Tétot *et al* 2008, Song *et al* 2010). This parameter has little effect on the resulting maximum crystal size, since changing γ by 100% causes a change in r_{max} of ~0.4%. The values found for the energy density, μ in the 3rd order term have a larger fractional effect on the final calculation of r_{max},; (changing μ by 100% gives a change in r_{max} of ~75%) however the spread of the μ values found from various studies are small and have a value of ~0.8 eV Å^{-3} with a fractional spread of 3% (Tétot *et al* 2008, Prasai *et al* 2012). Conversely, the novel 4th order term is strongly affected by the value of Y, and the density ratio ρ_c/ρ_a (equation (9)). The densities ρ_c of the crystalline phase for each material have well known values from literature and were kept fixed (Ottermann *et al* 1996, Alderman *et al* 2018, Aydin and Tokatas 2019).

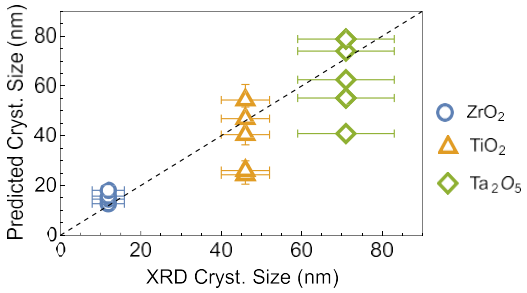

Figure 8. Plots the predicted maximum crystallite size from equation (11) using the pairs of material parameters in table 3 against the values for the average maximum crystallite sizes we measured, given in table 2.

Calculation for the predicted maximum crystallite sizes were made using pairs for Y, ρ_a that were found to be correlated i.e., from the same studies. Table 3 lists the parameters that we thus selected from literature and used to calculate the maximum size, and figure 8 shows the predicted maximum crystallite sizes plotted against the values from table 2. Crystal phase densities are gathered from (Berkeley Lab 2022). Results from the earlier, less precise study of tantala coating samples (mentioned in the introduction) are presented in figure 8 alongside the results of the titania and zirconia coatings. A more careful study of tantala will be performed, but the observed maximum sizes are presented since they are, within error, on the order of those predicted by equation (11). The physical parameters found in literature for tantala are included in table 3, since they are used to calculate the predicted maximum crystallite sizes shown in figure 8.

8. Possible implications

Off-axis photographs of one the LIGO test masses with the full 3 kW of standing light power incident on the surface shows on the order of 10^5 scattering points within the beam spot (Glover *et al* 2018). These objects detected at a wide scatter angle must be subwavelength in size.

Even though the LIGO coatings had been annealed below the threshold temperature, results presented here suggest that a small, undetected but significant population of crystallites may have been present and responsible for the observed scattering.

Measurements of the test mass coatings (Yamamoto 2007) showed ~10 ppm scattered power at wide angle. Applying the Rayleigh scattering cross section to the limited sized crystallites (Hulst and van de Hulst 1957)

$$C_{\text{scatter}} = \frac{32}{7}(m-1)^2 \frac{16\pi^5 d^6}{\lambda^4} \tag{12}$$

and multiplying by the number density of scatterers observed by Glover, results in a prediction of 0.1 ppb to 1 ppm scattered power. This is less than the ~10 ppm reported by Yamamoto, but one should also consider the following factors,

(1) Index of refraction. The Rayleigh scattering depends on the relative index of refraction, m of the crystallite in the amorphous medium of the coating. This value is not well defined for the model we present of crystallites which are strained at the interface with the amorphous matrix.

(2) Size. The d^6 dependence in the scattering cross section is highly sensitive to the crystallite size, and we do not know the scale of the crystallites in the titania doped tantala coatings deposited on the LIGO test masses.
(3) Crystallization is a stochastic process. The XRD-determined size of a crystallite is only sensitive to perfectly periodic structures. The cross section in the optical domain may be larger due to a chaotic halo of partially crystallized, and hence denser, material surrounding the perfectly crystallized core. This additional layer may be optically effective but invisible to x-ray detection.

These considerations make the scattering calculated from the crystallites not inconsistent with the measured values.

The fraction of scattered power becomes increasingly important in the interferometric detection of future gravitational wave detectors which require larger standing light power.

Highly reflective coatings can be manufactured with stacks of nano-layers adding up to $^1/_4$ wavelength thicknesses while achieving the same reflectivity. These nano-layered coatings have been shown to depress crystallization and may limit the number and size of crystallites. Improvement of the experimental methods and refinement of the theoretical models presented here will provide more insight into mitigation of the problem of light scatter in high precision optical coatings.

If the crystallites are confirmed to be the main source of wide angle scattering and the chaotic halo turns out to also generate mechanical dissipation, crystallite suppression will also result in thermal noise reduction.

9. Conclusion

For the titania and zirconia deposited metal oxide samples, we observed that roughly 50% of the deposited amorphous material does not crystallize even at the highest (∼700 °C) annealing temperatures measured. We found that a fraction of the coating's amorphous component was present in the zirconia and titania samples at all annealing temperatures.

The limited crystallite sizes growing from an amorphous, rigid medium can be explained by adding a 4th order term in the Gibb's free energy expression derived from the shell of strain which emerges at the interfaces of a denser crystallite growing into a rigid amorphous matrix. Within uncertainties the calculated limit sizes predicted by the expression agree with measurements. The strained amorphous matrix surrounding these crystallites may explain why we did not observe 'full' crystallization of the samples at temperatures higher than the crystallization threshold.

The observation that the crystallites grow to the limit size immediately at the annealing threshold temperature coupled with the small increase of the crystallized phase signal, (while the amorphous fraction decreases) at higher temperatures suggests that increasing annealing temperatures result in an increase in the number of crystallites, not their sizes. The fraction of amorphous phase surviving in all cases indicates that crystallization may be nucleation limited.

The limits of our XRD detection sensitivity, 3%–5% of the largest saturated crystallization peaks observed, along with the studies (Sengottaiyan *et al* 2019) using TEM images of a thin film with crystalline structures below XRD detection threshold, suggests that a small population of undetectable crystallites may exist in most coatings even below the crystallization threshold temperature.

Data availability statement

All data that support the findings of this study are included within the article (and any supplementary files).

Acknowledgments

We acknowledge the support from California State University Los Angeles CCR grants, NSF awards 2011710 and 2309294.

Conflict of interest

The authors declare no conflicts of interest.

ORCID iD

Seth Linker https://orcid.org/0000-0002-6762-0525

References

Acernese F *et al* 2014 Advanced Virgo: a second-generation interferometric gravitational wave detector *Class. Quantum Grav.* **32** 024001

Alderman O L, Benmore C J , Neuefeind J, Coillet E, Mermet A, Martinez V, Tamalonis A and Weber R 2018 Amorphous tantala and its relationship with the molten state *Phys. Rev. Mater.* **2** 043602

Anderson O *et al* 1997 Density and Young's modulus of thin TiO_2 films *Fresenius`J. Anal. Chem.* **358** 315–8

Ando M TAMA collaboration 2005 Current status of the TAMA300 gravitational-wave detector *Class. Quantum Grav.* **22** S881–9

Aso Y, Michimura Y, Somiya K, Ando M, Miyakawa O, Sekiguchi T, Tatsumi D and Yamamoto H 2013 Interferometer design of the KAGRA gravitational wave detector *Phys. Rev.* D **88** 043007

Aydin H and Tokatas G 2019 Characterization and production of slip casts mullite–zirconia composites *SN Appl. Sci.* **1** 1–15

Berkeley Lab 2022 *Material Explorer (The Materials Project)* (available at: https://next-gen.materialsproject.org/materials/) (Accessed 3 November 2023)

David W I F 1986 Powder diffraction peak shapes. Parameterization of the pseudo-Voigt as a Voigt function *J. Appl. Crystallogr.* **19** 63–64

Favaro G 2023 Virgo DCC (DCC-G2301569) (https://doi.org/10.1038/s41598-023-46101-3)

Glover L *et al* 2018 Optical scattering measurements and implications on thermal noise in gravitational wave detectors test-mass coatings *Phys. Lett.* A **382** 2259–64

Granata M *et al* 2020 Amorphous optical coatings of present gravitational-wave interferometers *Class. Quantum Grav.* **37** 095004

Grote H (Forthe LIGO Scientific Collaboration) 2010 The GEO 600 status *Class. Quantum Grav.* **27** 084003

Harry G B 2012 *Optical Coatings and Thermal Noise in Precision Measurement* (Cambridge University Press)

Harry G M Forthe LIGO Scientific Collaboration 2010 Advanced LIGO: the next generation of gravitational wave detectors *Class. Quantum Grav.* **27** 084006

Hulst H C and van de Hulst H C 1957 *Light Scattering by Small Particles* (Wiley)

Jian Z and Hejing W 2003 The physical meanings of 5 basic parameters for an x-ray diffraction peak and their application *Chin. J. Geochem.* **22** 38–44

Koski K, Hölsä J and Juliet P 1999 Properties of zirconium oxide thin films deposited by pulsed reactive magnetron sputtering *Surf. Coat. Technol.* **120** 303–12

Langford J I *et al* 1978 Scherrer after sixty years: a survey and some new results in the determination of crystallite size *J. Appl. Crystallogr.* **11** 102–13
Lv Q H 2018 Effects of annealing on residual stress in Ta_2O_5 films deposited by dual ion beam sputtering *Coatings* **8** 150
Martin I W *et al* 2010 Effect of heat treatment on mechanical dissipation in Ta_2O_5 coatings *Class. Quantum Grav.* **27** 225020
Nastasi M, Mayer J and Hirvonen J 1996 *Ion-Solid Interactions: Fundamentals and Applications* (*Cambridge Solid State Science Series*) section 7.11 (Cambridge University Press)
Neilson J 2022 Nanolayered optical coatings for the mirrors of interferometric gravitational-wave detectors: deposition and characterization *LIGO Document Control Center* (available at: https://dcc.ligo.org/LIGO-P2200081) (Accessed 25 June 2023)
Nie X, Ma F, Ma D and Xu K 2015 Thermodynamics and kinetic behaviors of thickness-dependent crystallization in high-k thin films deposited by atomic layer deposition *J. Vac. Sci. Technol.* A **33** 01A140
Ottermann C R *et al* 1996 Young's modulus and density of thin TiO_2 films produced by different methods *MRS Online Proc. Libr. (OPL)* **436** 251
Prasai B, Cai B, Underwood M K, Lewis J P and Drabold D A 2012 Properties of amorphous and crystalline titanium dioxide from first principles *J. Mater. Sci.* **47** 7515–21
Ramirez L, Mecartney M L and Krumdieck S P 2008 Nanocrystalline ZrO_2 thin films on silicon fabricated by pulsed-pressure metalorganic chemical vapor deposition (PP-MOCVD) *J. Mater. Res.* **23** 2202–11
Sengottaiyan R *et al* 2019 Temperature dependent structural evolution and crystallization properties of thin $Ge_{15}Te_{85}$ film revealed by in situ resistance, x-ray diffraction and scanning electron microscopic studies *J. Phys. D: Appl. Phys.* **53** 025108
Siltronix n.d. *Siltronix Silicon Wafers* (available at: www.sil-tronix-st.com) (Accessed 11 March 2020)
Song D-P, Chen M-J, Liang Y-C, Wu C-Y, Xie Z-J and Bai Q-S 2010 Molecular dynamics simulation study on surface structure and surface energy of anatase *Modelling Simul. Mater. Sci. Eng.* **18** 075002
Tétot R, Hallil A, Creuze J and Braems I 2008 Tight-binding variable-charge model for insulating oxides: application to TiO_2 and ZrO_2 polymorphs *Europhys. Lett.* **83** 40001
Yamamoto H 2007 LIGO I mirror scattering loss by non smooth surface structure *LIGO DCC Document 70170*
Youhong L *et al* 2003 Embedded-atom-method tantalum potential developed by the force-matching method *Phys. Rev.* B **67** 125101